A&A 431, 879–886 (2005)
DOI: 10.1051/0004-6361:20041541

Astronomy & Astrophysics

Q0957+561 revised: CO emission from a disk at $z = 1.4$⋆

M. Krips[1,2], R. Neri[2], A. Eckart[1], D. Downes[2], J. Martín-Pintado[3], and P. Planesas[4]

[1] I. Physikalisches Institut, University of Cologne, Zülpicherstr. 77, 50937 Köln, Germany
e-mail: krips@ph1.uni-koeln.de
[2] Institut de Radio Astronomie Millimétrique, 300 rue de la Piscine, 38406 Saint Martin d'Hères, France
[3] Instituto de Estructura de la Materia (CSIC), Serrano 121, 28006 Madrid, Spain
[4] Observatorio Astronómico Nacional (IGN), Apartado 112, 28800 Alcalá de Henares, Spain

Received 28 June 2004 / Accepted 19 October 2004

Abstract. Based on additional interferometric observations, we reanalysed the CO(2−1) and 3 mm continuum emission of Q0957+561, a lensed QSO at a redshift of $z = 1.4141$. The emission in the CO(2−1) lines reveals a gas-rich host galaxy with a peculiar double-peaked profile at one of the two lensed images. Our new interferometric CO maps of the host galaxy agree well with HST images obtained by Keeton et al. (2000) and we thus argue that the two velocity components arise from molecular gas in the disk of the host galaxy. We also present new model calculations, all in excellent agreement with recent time delay measurements and simulations.

Key words. gravitational lensing – Galaxy: kinematics and dynamics – galaxies: quasars: individual: Q0957+561 – galaxies: high redshift – Galaxy: disk

1. Introduction

Since the discovery of Q0957+561, the first confirmed gravitationally lensed quasar (Walsh et al. 1979) at a redshift of $z = 1.4141$, several models have been developed to understand the lensing potential of the intervening galaxies: a giant elliptical galaxy (G1) at a redshift of $z = 0.355$ with a surrounding cluster and probably another group of background galaxies at $z = 0.5$ (Angonin-Willaime et al. 1994; Chartas et al. 1998). Besides flux amplification, gravitational lensing helps also to improve spatial resolution as detailed by Kneib et al. (1998). Differential lensing effects which are detectable through the comparison of lensed images at different wavelengths indeed provide a powerful tool to probe the structure of a galaxy at a much higher resolution than possible with current millimeter interferometers. Planesas et al. (1999, in the following P99) have succeeded in detecting the CO(2−1) line in the host galaxy around Q0957+561, but lacked a detailed lensing model to investigate the source of molecular emission. Keeton et al. (2000) have recently detected also the stellar component of the host galaxy showing differences in its distribution with respect to those of the gas obtained by P99.

To confirm and substantiate the weak line profiles previously detected by P99 and to eliminate the previous inconsistencies to Keeton et al. (2000), we have carried out new observations with the IRAM interferometer. To further improve on P99's interpretation, we have developed a numerical code which incorporates existing lensing models of Q0957+561[1].

2. Observations

CO(2−1) and (5−4) observations of Q0957+561 were made simultaneously in 1998 and again in 2003 with the IRAM interferometer. The first observation run is discussed in P99. We only give additional details on the refined reduction of this data set.

Data taken in 1998: the observations were carried out in the B, C and D configurations. The bandwidth of the cross-correlator was set up to cover 420 MHz at both frequencies with a spectral resolution of 2.5 MHz, equivalent to 7.8 km s^{-1} at 95.5 GHz (redshifted CO(2−1)) and 3.1 km s^{-1} at 238.7 GHz (CO(5−4)). The bandpass was calibrated on 3C273, 3C345 or 0923+392 while phase and amplitude calibrations were performed on 0917+624. Unlike P99, we discarded data from an entire observing run that were substantially reducing the quality of the maps. We have also corrected for the velocity scale which was wrong by a factor of 1.5 in P99 due to a data header error.

Data taken in 2003: the observations were carried out in the C and D configurations. The bandwidth of the cross-correlator was set up to cover 580 MHz with a spectral

⋆ Based on observations carried out with the IRAM Plateau de Bure Interferometer. IRAM is supported by INSU/CNRS (France), MPG (Germany) and IGN (Spain).

[1] We adopt a flat cosmology with $\Omega_M = 0.3$, $\Omega_V = 0.7$ and a Hubble constant of 65 km s^{-1} Mpc^{-1}.

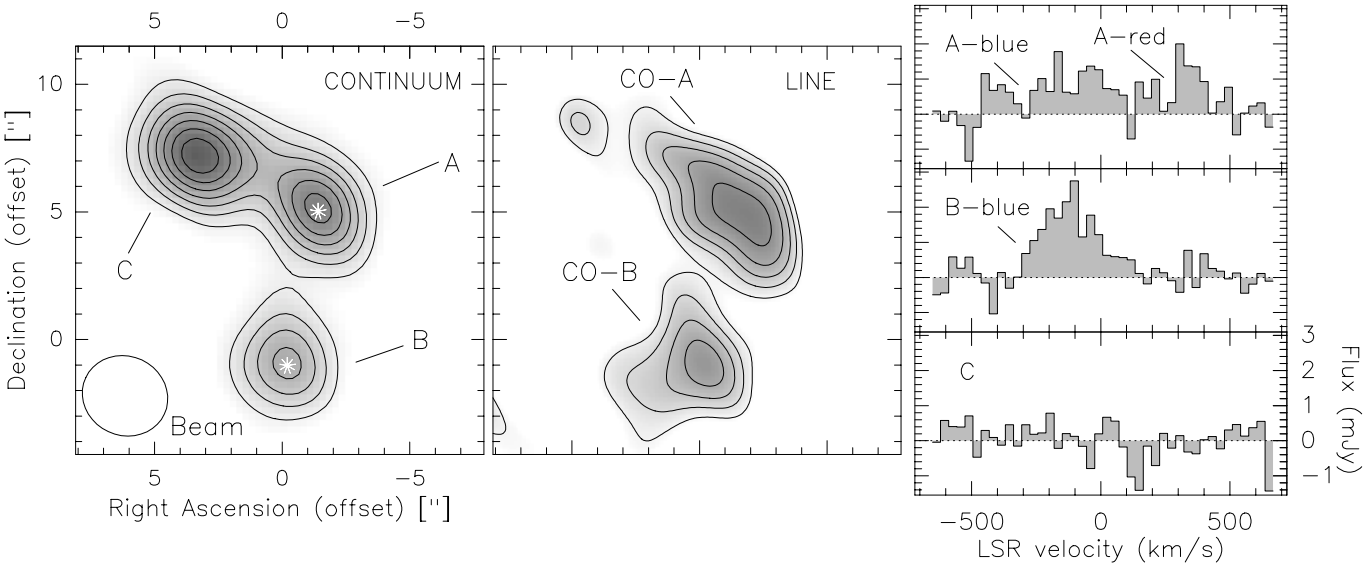

Fig. 1. Continuum at 3 mm (*left panel*), integrated CO(2–1) line emission (*middle panel*) and the spectral CO(2–1) profiles observed toward CO−A, CO−B and at the 3 mm position of the radio jet (*right panel*). Offset position (0, 0) is at the assumed position of the lens, i.e. at α_{J2000} = 10:01:21.0, δ_{J2000} =+55:53:50.5. Contour levels are from 5σ = 1.1 to 4.7 mJy beam^{-1} in steps of 0.6 mJy beam^{-1} for the 3.1 mm continuum and from 3σ = 0.33 to 0.77 Jy km s^{-1} in steps of 0.11 Jy km s^{-1} for the line emission. The synthesized beam of 3.2″ × 3.0″ at PA 87° is shown in the lower left corner (1″ corresponds to 9 kpc at an angular-size distance D_A = 1.87 Gpc). The white stars indicate the optical positions of the A and B image. The rms noise per 10 MHz channel is ∼0.65 mJy. The spectrum at the position of the jet is indicative of the noise level. Velocities are relative to the redshift at z = 1.4141.

resolution of 1.25 MHz corresponding to 3.9 km s^{-1} at 95.5 GHz and 1.6 km s^{-1} at 238.7 GHz. We resampled the two data sets to a spectral resolution of 7.8 km s^{-1} (2.5 MHz) over the 420 MHz band covered by the first observations to ensure uniform noise in the merged velocity channels. 3C 273, 0851+202 and 0420-014 were used as bandpass calibrators while 0804+499 and 1044+719 were taken as phase and amplitude calibrators. Relative to P99, the sensitivity of the combined data sets is now higher by a factor of ∼2.

3. The data

3.1. Continuum emission

3.1 mm: the radio continuum was computed separately for the two data sets by averaging the line-free channels with a velocity lower than −510 km s^{-1} and higher than +540 km s^{-1}. Two lensed images of the quasar, labeled A and B, and a radio jet C appear at this wavelength (Fig. 1), in agreement with VLA observations (Harvanek et al. 1997). The positions coincide with the optical ones within the errors (Table 1). Also in agreement with previous work, the A and B components are pointlike whereas the radio jet C component is slightly elongated (∼2.7″, PA ∼ 60°) in the beam of the interferometer. Finally, there is no evidence for variability above 10% between May 1998 and April 2003 in all three components. This coincides with results obtained at 3.6 cm with the VLA by Harvanek et al. (1997).

1.3 mm: a noise level of σ = 0.6 mJy was obtained in the 2003 data by averaging over the entire bandwidth available at 1.3 mm. We find a 3.5σ peak at the 3 mm position of the A-continuum component, a 2σ peak at the position of the B component and a 4σ peak at the position of C. The steep drop in flux density at 1.3 mm is consistent with the weakness of the synchrotron emission expected if we extrapolate to this short wavelength the spectral index of ≃−0.6 measured in the 20 mm (Harvanek et al. 1997) to 3 mm (P99, and this paper) range. Any dust emission is either too weak or too extended (say >3″) to be detected at this frequency. Data from the 1998 run were not taken into consideration as they were much less sensitive.

3.2. Line emission

CO(2−1): to estimate flux densities in the CO(2−1) line (Table 1), the 3.1 mm continuum was first removed separately from each data set to account for possible low level continuum variability. Then, all data sets were combined to a single uv-table, and velocity channels in the −510 km s^{-1} to +540 km s^{-1} range was summed to produce an integrated line map (Fig. 1). The resulting map shows two lensed images labeled CO−A and CO−B (P99). The emission centroids of the two images are separated by ≃7″, about 1″ more than in the optical, radio and millimeter continuum (Table 1). The spectral profiles taken towards positions CO−A and CO−B are different. While a double-peaked profile is visible towards the northern image CO−A, a single blueshifted velocity component is detected towards CO−B. The shape of the blue components measured towards CO−A and CO−B is similar. The CO−F image reported by P99 could not be confirmed with the new observations.

CO(5−4): no significant line emission was detected at the position of CO−A and CO−B, the two line components detected at 3 mm. A ∼1.9 mJy (=3σ) peak is only tentatively detected in the velocity integrated map (−300 km s^{-1} to +100 km s^{-1})

Table 1. Flux densities, velocities and positions of individual image components. Values have been determined by fitting Gaussian profiles to the visibilities. Offset position (0, 0) is at the assumed lens position specified in the caption of Fig. 1. [a] Relative position uncertainties are based on statistical noise and do not include astrometric errors. [b] Values taken from the second observation campaign in 2003. [c] Values in brackets are from the reanalysis of the P99 data, and do not include data from 2003. [d] Velocities are relative to the redshift at $z = 1.4141$. The CO(2−1) line parameters for the two A components were not derived from the spectrum shown in Fig. 4 that was taken *between* A-red and A-blue, but are based on spectra determined at the respective positions of A-blue and A-red.

	CO(2→1)			Continuum at 3.1 mm[b]		
	A-blue	A-red	B-blue	A	B	C
Rel. positions (″)	(−1.9, +3.8)	(−1.6, +6.1)	(+0.2, −1.1)	(−1.45, +5.00)	(−0.24, −1.0)	(3.23, 7.13)
Position errors (″)[a]	(+0.2, +0.2)	(+0.3, +0.3)	(+0.2, +0.2)	(+0.06, +0.08)	(+0.08, +0.10)	(+0.07, +0.08)
Flux density (mJy)	–	–	–	4.7 ± 0.2	3.4 ± 0.2	6.2 ± 0.2
Peak flux[c] (mJy/beam)	0.9 ± 0.2	2.1 ± 0.2	2.2 ± 0.2	4.6 ± 0.2	3.3 ± 0.2	5.1 ± 0.2
	(1.1 ± 0.3)	(1.7 ± 0.3)	(2.3 ± 0.3)	(4.2 ± 0.3)	(2.5 ± 0.3)	(5.5 ± 0.3)
FWHM (km s^{-1})	280 ± 60	160 ± 20	280 ± 50	–	–	–
Vel. at line peak[d] (km s^{-1})	−140 ± 30	340 ± 15	−140 ± 23	–	–	–
Integr. line flux (Jy km s^{-1})	0.25 ± 0.06	0.34 ± 0.06	0.61 ± 0.06	–	–	–

at the position of CO−B. The intensity of the CO−B component at 3 mm over the same velocity range is estimated to be 1.8 mJy. Although uncertain because of the low signal to noise ratio of the (5−4) line, and possibly because of some residual continuum emission, we set an upper limit of ≤1 on the velocity averaged intensity ratio R_{54} = CO(5−4)/CO(2−1) toward CO−B, the strongest of the two line components.

4. Modelling Q0957+561

We developed a numerical code based on the standard gravitational lens equation (Schneider et al. 1992) to explain the absence of the double-peaked line profile toward CO−B and to investigate the distribution and kinematics of the molecular gas around Q0957+561.

The code has been applied on 6 different models of Q0957+561 (Table 2), all based on previous work by Barkana et al. (1999) and Chae et al. (1999). The mass distributions of three models are based on King profiles, as proposed by Falco et al. (1985-models: FGS, FGSE, FGSE+CL), the remaining three on a softened power-law distribution, as suggested by Grogin et al. (1996-models: SPLS, SPEMD, SPEMD+CL). FGS and SPLS are spherical models where the effects of the surrounding cluster at $z = 0.355$ are approximated by an external shear. FGSE and SPEMD models take into account the ellipticity in the lens galaxy, the remaining models use a single isothermal sphere (SIS) to model the lens properties of the cluster (SPEMD+CL, FGSE+CL). A point mass was added to the King profiles to account for a black hole in the center of the lens galaxy (Mediavilla et al. 2000; Barkana et al. 1999), except for the softened power law models which implicitely cover this case. The group of background galaxies at $z = 0.5$ has not been considered, however. The composite pseudo-Jaffe models by Keeton et al. (2000) have not been taken into account as they would not have provided further details for our analysis.

To find the set of parameters for each model reproducing our observations with the lowest χ^2_r, we first restricted the parameter space with simple assumptions based on the number of lensed images, separations among them etc. We then scanned the parameter space for each model to get the lowest χ^2_r and included the following constraints: relative positions of the A and B continuum components at 3.1 mm with respect to the lens (4 constraints), relative positions of CO−A-blue and CO−B-blue (Table 1), the continuum and line intensity ratios and the optical/radio time delay of 400−420 days from Kundic et al. (1997) and Haarsma et al. (1999). This results in a total of 11 constraints. For simplicity, compact fixed-size Gaussians were used to approximate the respective components. The so found best-fit models turned out to be in excellent agreement with simulations based on VLA and optical data (e.g. Barkana et al. 1999; Chae et al. 1999; Keeton et al. 2000).

The SPEMD+CL, FGSE+CL and the FGS models reproduce the observed constraints with the lowest χ^2_r (≤3; Table 2). Although the FGS model yields one of the best results, we do not favour spherical mass distributions because of the ellipticity of the lens (Bernstein et al. 1997). The contribution of the cluster is also important: The models that best explain these observations all require an SIS cluster (FGSE+CL and SPEMD+CL, the latter has a lower χ^2)[2]. We note that the time delay derived from the same models are in rather good agreement with recent optical and radio measurements (∼400−420 days; Kundic et al. 1997; Haarsma et al. 1999).

4.1. Line emission

In the following two subsections we discuss different approaches for modelling the blueshifted line emission based on the best-fit FGSE+CL potential and then explain the difference seen in the profiles toward CO−A and CO−B.

[2] For the following discussion, we will mainly use the best-fit FGSE+CL model since it provides the closest match to already published results, e.g. Keeton et al. (2000). However, both models are fully equivalent for argumentation purposes.

Table 2. Best fit parameters for Q0975+561. Parameters are: $\Delta\alpha \equiv$ right ascension, $\Delta\delta \equiv$ declination, $\sigma \equiv$ velocity dispersion, $\xi_c \equiv$ core radius, $\varepsilon \equiv$ ellipticity, $\Phi_{PA} \equiv$ position angle, $\eta \equiv$ power law index, $\gamma^{(\prime)} \equiv$ shear term, $\Phi_\gamma \equiv$ shear angle, $M_{bh} \equiv$ mass of the black hole, $\Delta\tau \equiv$ time delay, $m \equiv$ magnification factor. [a] Offset from assumed lens position. [b] Fixed parameters (shown in *italic*). [c] Values in brackets are χ^2_r-tests with time delay. The reduced χ^2_r is defined as: $\chi^2_r = \chi^2/N_{d.o.f.}$ where $N_{d.o.f.}$ is the degrees of freedom. [d] γ' is only taken for the elliptical potentials ($\gamma' = \gamma/(1-\kappa)$) where $\kappa = \Sigma_{clus}/\Sigma_{crit}$ is defined as the surface mass density of the cluster in units of the critical surface density (Barkana et al. 1999). For the spherical models, $\kappa = 0$ and for the elliptical ones it can be approximated by $\kappa \simeq \gamma$, i.e. $\gamma' = \gamma/(1-\gamma)$. [e] based on Barkana et al. (1999). [f] Based on Chae et al. (1999). [g] Determined for the blue component.

	SPLS [e]	SPEMD [e]	SPEMD+CL [f]	FGS [e]	FGSE [e]	FGSE+CL [e]
Source Positions						
(Source plane)						
Radio continuum						
$(\Delta\alpha_s, \Delta\delta_s)$ ($''$) [a]	(−0.02, 0.90)	(−0.14, 1.02)	(2.20, 2.49)	(−0.15, 1.06)	(−0.18, 1.10)	(1.80, 2.58)
Line emission						
$(\Delta\alpha_s, \Delta\delta_s)$ ($''$) [a]	(−0.23, 0.95)	(−0.32, 1.00)	(1.93, 2.39)	(−0.38, 1.05)	(−0.40, 1.05)	(1.54, 2.47)
Lens properties						
Galaxy:						
σ_v (km s^{-1})	400	400	360	300	340	320
ξ_c ($''$)	0.12	0.12	0.02	1.2	0.6	1.1
ε	–	0.1	0.2	–	0.1	0.3
Φ_{PA} (°) [b]	–	*64*	*64*	–	*64*	*64*
η	1.1	1.0	1.1	–	–	–
Cluster:						
γ' [d]	0.3	0.2	–	0.4	0.3	–
$\Phi_{\gamma'}$ (°) [b]	*60*	*60*	–	*60*	*60*	–
σ_{cl} (km s^{-1})	–	–	375	–	–	350
$(\Delta\alpha_{cl}, \Delta\delta_{cl})$ ($''$) [b]	–	–	*(13.7, 6.9)*	–	–	*(13.7, 6.9)*
Black hole:						
M_{bh} (10^{12} $M_\odot$)	–	–	–	0.5	0.3	0.2
$\Delta\tau_{cont}$ [days]	411	420	417	417	421	416
$\Delta\tau_{line}$ [days] [g]	421	450	412	423	454	414
m^{total}_{RC}	5	4	4	3	3	3
m^{total}_{CO}	6	7	9	5	6	6
$N_{d.o.f.}$ [c]	3	2	2	3	2	2
χ^2_r [c]	3.0 (3.4)	5.5 (40)	1.5 (1.5)	1.3 (1.2)	5 (40)	2.0 (2.5)

4.1.1. The blueshifted line

Let us first concentrate on the blueshifted line. We can propose two different scenarios for the origin of blueshifted line emission:

- a compact or extended[3] region centered on the nucleus,
- a compact or extended region spatially not coincident with the nucleus.

The small line ratio A-blue/B-blue of ∼0.4 already rules out a compact region centered on the nucleus, since it disagrees with the measured 3 mm continuum ratio A/B of 1.5 ± 0.1. Even if we account for a contribution of the jet in the A component and assume a lower ratio for the core emission at 3 mm, we know from VLBI observations that the ratio A/B at the core is close to 1.3 (Garret et al. 1994). Thus, the continuum at 3 mm and the blueshifted CO emission cannot originate from the same compact region (compare also Fig. 2).

On the other hand, an extended line emitting region centered on the nucleus can indeed result in an A-blue/B-blue of 0.4. To constrain the size of the blueshifted region, we assumed an elliptical Gaussian profile and fitted the full widths at half maximum (*FWHM*) and the position angle (PA) depending on the continuum and line ratios between the lensed images. A best-fit (Fig. 3) is obtained for a disk-like region, that is extended in the direction of the nuclear jet (∼5″) and tiny in the direction perpendicular to the jet (∼0.2″, PA = 20°), with the south-western part of the disk crossing the inner tangential

[3] Simulated by an elliptical Gaussian profile, i.e. a distribution which is symmetric with respect to its centroid.

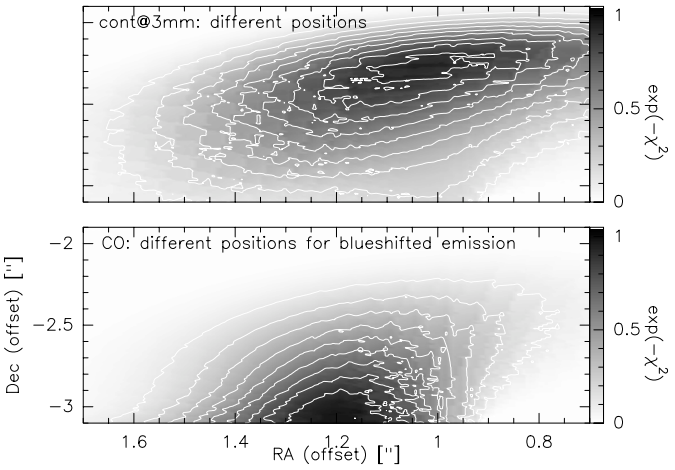

Fig. 2. χ^2 results for the continuum (*upper panel*) and blueshifted line (*lower panel*) position fits based on the FGSE+CL model. Shown here are different positions in the source plane for the blueshifted line emission and the continuum depending on the χ^2-test including the observed intensity ratios between the two lensed images and the observed position. Assumed values for the 3 mm continuum: A/B = 1.5; blueshifted line: A/B = 0.4. Positions for the A, B (continuum) and CO−A and CO−B can be found in Table 1. Contour levels are from 0.1 to 1.0 in steps of 0.1. The region with a value close to 1.0 in this map corresponds to the best-fit position.

caustic of the lens. A priori, such a model produces multiple images (up to 5; compare also Keeton et al. 2000) that result in a stronger CO−B image.

Alternatively to the extended region centered on the nucleus, blueshifted emission from a rather *compact* region (<1″) close to the inner tangential caustic and slightly off (∼0.5″ to the south-west) the nuclear position is also consistent with a line ratio of ∼0.4 (Fig. 3). A symmetric *extended* region (>1″) at an off-nuclear position does not produce such a low A-blue/B-blue of 0.4.

Thus, an independent blueshifted emission must either originate in an extended region centered on the nucleus or in a compact region with a position close to the tangential caustic.

4.1.2. The redshifted line

The difference in the line profiles observed toward CO−A and CO−B can be explained by the location of the redshifted gas component relative to the lens caustic. The best-fit simulation for the FGSE+CL model produces one tangential caustic (Fig. 4). The radial caustic is at infinity. While the continuum and blueshifted line components remain close to the tangential caustic and are thus deflected into two distinct images, the redshifted component is already located too far off the caustic (to the north-east) to generate two lensed images. Thus, it appears that both blue- and redshifted gas become visible toward CO−A while blueshifted gas only can be detected toward CO−B. The unlensed separation between the centroids of the blue- and the redshifted components, corrected for magnification, are estimated to ∼1″, or equivalently ∼9 kpc at the distance of Q0957+561.

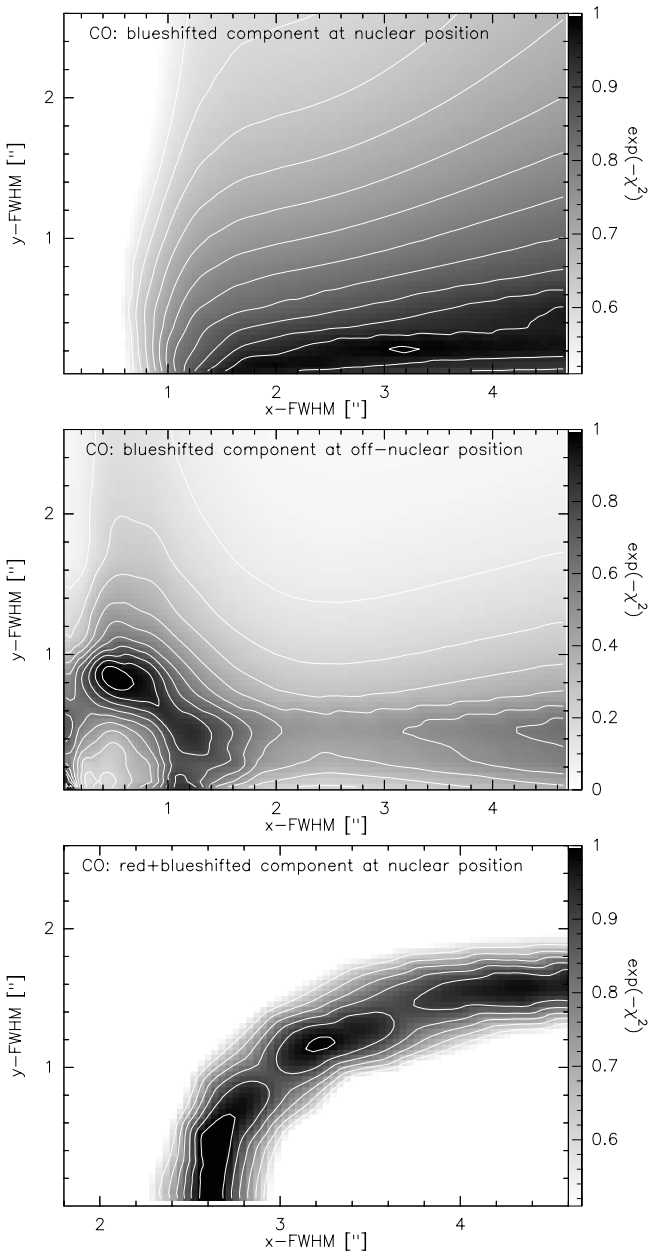

Fig. 3. χ^2 results of the size fit for the line emission. The FWHM of the Gaussian profile are plotted with the respective χ^2. We also varied the position angle (PA) from 5 to 60° but we restricted the presentation to the PA with the lowest χ^2. *Upper panel*: blueshifted emission centered on the nucleus. χ^2 values based on the A-blue/B-blue ratio. Lowest χ^2 for PA = 20°. Contour levels start at 0.56 to 1.0 in steps of 0.04. *Middle panel*: blueshifted emission centered at a fixed off-nuclear position closer to the tangential caustic (≡position of line emission in Table 2). χ^2 based on the A-blue/B-blue ratio. Lowest χ^2 for PA = 20°. Contour levels are from 0.1 to 1.0 by 0.1. *Lower panel*: red- and blueshifted emission centered on the nucleus. χ^2 values based on the (A-blue+A-red)/B-blue ratio. PAs of 50 ± 10° all result in a low χ^2. Contour levels are from 0.6 to 1.0 in steps of 0.08.

Likewise, an extended region centered on the nucleus where the north-eastern part corresponds to the redshifted component and the south-western part to the blueshifted one produces equivalent results (Fig. 3). To obtain the derived line ratio

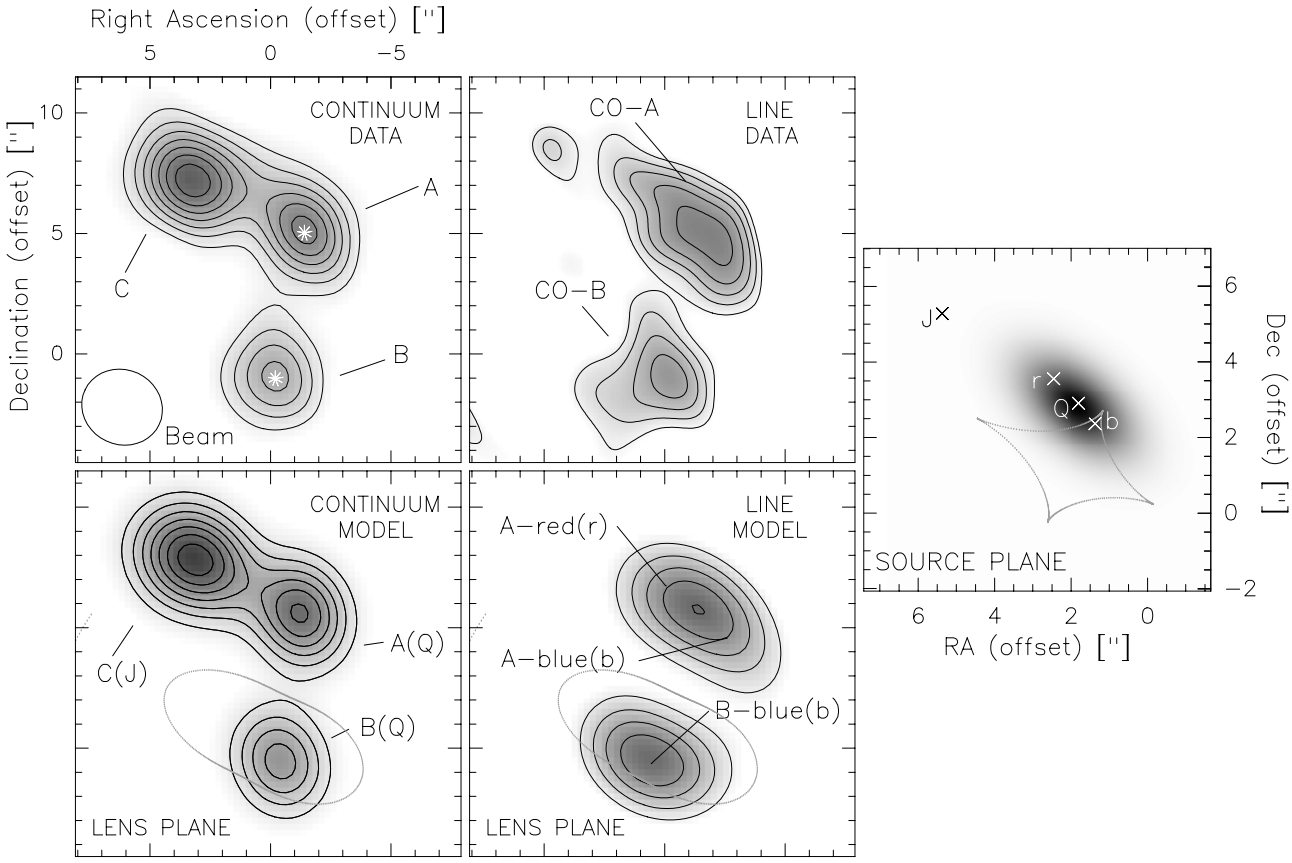

Fig. 4. The line-free continuum at 95 GHz (*upper left panel*) and the ^{12}CO(2→1) line emission (*upper middle panel*) as observed with the IRAM interferometer from both data sets. The lower panels show the *simulated* radio continuum (*left*) and line emission (*middle*) convolved with the synthesized beam and the critical lines (*grey lines*). In the *right* panel the location of the *unlensed* line emissions (r ≡ A-red, b ≡ B-blue ≡ A-blue) as well as the *unlensed* radio continuum (J ≡ jet, Q ≡ quasar) is shown together with the radial and tangential caustics with respect to the assumed position of the lensing galaxy (*grey lines*). The offset position (0, 0) of each map corresponds to the position of the lensing galaxy. Contour levels for the data are as Fig. 1. We have also used the same contour levels for the simulated maps. The white stars indicate the optical positions of the A and B image. The parameters used for the model (FGSE+CL) are listed in Table 2. Changes in the velocity dispersion of the lens of ∼1% or in the source positions of ∼0.1″ produce a difference in the time delay of the FGSE+CL model of ∼5%.

(A-blue+A-red)/B-Blue ∼1.0, the size of the region has to be extended by about ∼3−4″. This value seems to be independent of the lens potential even if we find that the SPEMD+CL model appears to favour slightly more elliptical profiles for the emission than the FGSE+CL model (cf. also Keeton et al. 2000). If we divide the lensed CO−A into a red- and blueshifted part and derive then the ratio between A-blue and B-blue, we again obtain a value of ∼0.4[4].

The sensitivity is not sufficiently high to establish the absolute genuineness of the CO−A-blue component from the observations alone, but our best-fit FGSE+CL model of the host galaxy not only agrees with the Barkana model of Keeton et al. (2000), but a priori corroborates the detection of blueshifted CO gas in the direction of component A.

[4] In contrast to Sect. 4.1.1, where we found that an extended blueshifted emission region would not result in an A-blue/B-blue ratio of 0.4 if symmetrically centered on a position closer to the tangential caustic, the extended emission region for the blueshifted part is not symmetric with respect to the position used there. This might explain why we nevertheless obtain such a low ratio for the blueshifted part alone.

4.2. Radio continuum

The morphology and the intensity ratios of the radio continuum can easily be modelled. As already noted by Schneider et al. (1992), the radio jet J is lensed only once due to its location far off the caustic.

5. Discussion

The 3 mm continuum observations of the redshifted double quasar Q0957+561 are in good agreement with observations at other wavelengths. While the 3 mm continuum emission from the quasar is unresolved, emission from the radio lobes is extended along the direction of the jet. The CO(2−1) line, however, does not originate in the quasar. The difference in position, and therefore in the deflection, explains also the difference between the flux density ratios in the 3 mm continuum (A/B = 1.5 i.e. like in the radio continuum) and in the line (CO−A/CO−B = 0.4 for the blue component), and accounts for different time delays for the CO(2−1) and the radio images. We note, however, that the time delay difference is only marginally significant (at most 5−20 light days, according to the models).

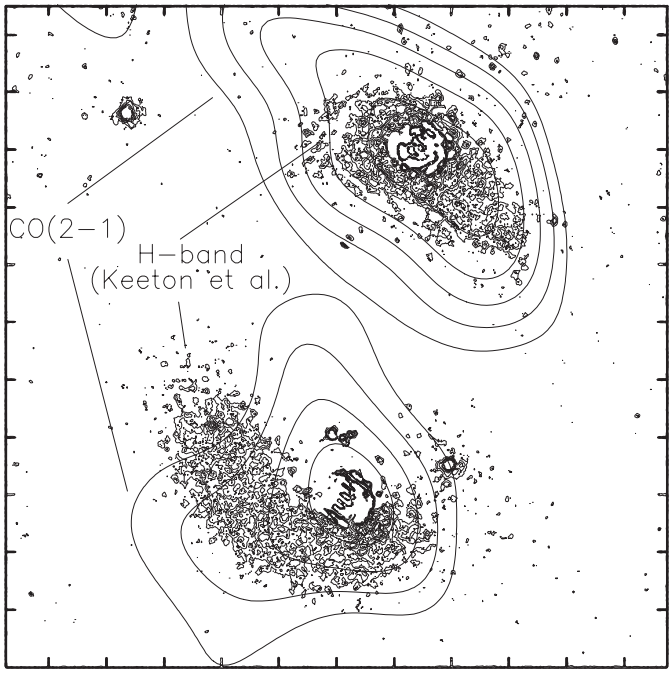

Fig. 5. HST image in the H-band of the host galaxy in Q0957+561 (Keeton et al. 2000) with contour levels from Fig. 4 of the velocity integrated CO(2−1) emission. Separation of the tick marks is 1″.

What can we conclude about the origin of the redshifted CO(2−1) velocity component? P99 argued that it was either originating from a companion galaxy, very close to Q0957+561 (see also Papadopoulos et al. 2001) or tracing the presence of molecular gas in the rotating disk of the host galaxy. Our models discard the first hypothesis. First, there has been no detection of such a companion galaxy at other wavelengths, but the host galaxy, which has already been revealed in HST observations by Keeton et al. (2000), is oriented in the direction of the two line components in CO−A and appears to be extended by ∼3″ (Fig. 5). Furthermore, models for the gas emission in the host galaxy that take the velocity profiles observed toward CO−A and CO−B into account are similar in size and shape (see Fig. 4) to those invoked by Keeton et al. (2000). The blue- and redshifted CO(2−1) emission appear to be very likely connected to the stellar distribution of the host galaxy and thus corroborate the results of Keeton et al. (2000), whereas models based on a single blueshifted component favour a very thin, elongated disk or a compact CO(2−1) emitting region slightly off the nuclear region, and as such are rather in contrast with images of the host galaxy. Moreover, the integrated line ratio (CO−A-red+CO−A-blue)/CO−B ∼ 1.0 is consistent with the ratio H-band-A/H-band-B ∼ 1 derived by Keeton et al. (2000). This is what one would expect if the profile of the gas distribution is very similar to the stellar one. Also, the double-peaked line profile at CO−A which appears to be symmetric and centered within the errors at $z = 1.4141$ is a classical signature for rotation and therefore, provides further support that the CO emission is associated with the host galaxy. By the same arguments we are tempted to exclude also a recent galaxy merger in Q0957+561, though this possibility cannot be ruled out completely.

Table 3. Apparent CO luminosity L' and molecular gas mass $M_{\rm gas}$ of Q0957+561. [a] m ≡ magnification factor. [b] determined with the FGSE+CL model.

	CO−A-red	CO−A-blue	CO−B-blue
$mL'_{\rm CO}$ [a]			
(10^{10} K km s^{-1} pc^2)	0.8 ± 0.3	0.8 ± 0.2	1.8 ± 0.2
$m_{\rm FGSE+CL}$ [b]	1.5	1.7	4.3
$M_{\rm gas}$ (10^{10} $M_\odot$)	2.7 ± 1.0	2.4 ± 0.6	2.3 ± 0.6
Total gas mass	$M^{\rm tot}_{\rm gas} \equiv M^{\rm red}_{\rm gas} + M^{\rm blue}_{\rm gas} \simeq 5 \times 10^{10}\ M_\odot$		

Based on these arguments, we favour P99's second hypothesis: the presence of an important reservoir of molecular gas in the disk of the host galaxy surrounding Q0957+561.

According to the models the continuum is less magnified by a factor of 2−3 relative to the strongly lensed optical images (∼10) while the total magnification factor derived in the CO line varies between $m^{\rm total}_{\rm CO} \simeq 6$ (FGSE+CL) and $m^{\rm total}_{\rm CO} \simeq 8$ (SPEMD+CL). Based on the lower magnification, we have estimated an upper limit to the molecular gas mass for the integrated blue- and redshifted velocity profile in CO−A and CO−B. The FGSE+CL model corresponds to the higher CO−luminosity case and provides therefore a slightly higher molecular gas mass. Under the assumption that the brightness temperature of the (1−0) and (2−1) lines is the same, we adopt a CO to H_2 conversion factor of $\simeq 4.8\,M_\odot$ (K km s^{-1} pc^2)$^{-1}$ based on a determination for the Milky Way (Solomon & Barrett 1991). Clearly, the Milky Way and the Q0957+561 host galaxy are in different evolutionary stages and show different properties, so the adopted conversion factor is likely to be an overestimate (cf. Downes et al. 1993), and an upper limit for the molecular gas mass will be obtained. Based on the FGSE+CL magnification factor, we estimate $M_{\rm gas} = M(H_2{+}He) \simeq 2.4 \times 10^{10}\ M_\odot$ for the blue profile and $\sim 2.7 \times 10^{10}\ M_\odot$ for the reddened profile ($\simeq 9 \times 10^9\ M_\odot$ for SPEMD+CL), giving an upper limit for the total gas mass of $\simeq 5.1 \times 10^{10}\ M_\odot$. We can also give a lower limit for the gas mass of $M_{\rm gas} \sim 8 \times 10^9\ M_\odot$ assuming that the CO(1−0) line is optically thin (Solomon et al. 1997). This relatively small difference of only a factor of 6 indicates that the standard conversion factor might nevertheless already give a reliable estimate of the gas mass in the host galaxy around Q0957+561. Assuming a radius of ∼10 kpc and a velocity separation between both line profiles of ∼400 km s^{-1}, we find a dynamical mass of $\sim 4 \times 10^{11}\ M_\odot$ (not including inclination effects). This is about ten times higher than the derived gas mass consistent with what is found for other active galaxies (e.g. Evans et al. 2002; Sakamoto et al. 1999). The low upper limit on the velocity-averaged line intensity ratio, $R_{54} \simeq 1$, favours the hypothesis of low excitation CO emitted mainly from the disk of the host galaxy. The agreement between molecular gas masses obtained with the integrated CO luminosities and individual magnification factors, each tracing line emission from half of the quasar host, is further support for the rotating disk hypothesis. If our assumptions are correct, the molecular gas in the disk cannot be very hot, but to our knowledge no sensitive observations in the ground and

higher rotational CO transitions have been carried out yet to confirm this conclusion.

6. Conclusions

Recent sensitive observations were combined with earlier data by Planesas et al. (1999) to corroborate their original discovery of CO(2−1) line emission from Q0957+561. A numerical program was developed to analyse the properties of the lensed system, the results of which can be summarized as follows. While the region of blueshifted line emission is found to lie in between the two caustics, and is therefore deflected into two images, redshifted emission is found outside the caustics, and therefore results in a single lensed image. We further argue that both redshifted and blueshifted line emission originate from the same system: a disk with a molecular gas mass of $\simeq 1-5 \times 10^{10}\ M_{\odot}$ in the host galaxy in Q0957+561. Our results for the host galaxy are in excellent agreement with a previous optical work by Keeton et al. (2000). To our knowledge HR10 (Andreani et al. 2000) and Q0957+561 are the only systems at redshifts of $1 < z < 2$ in which CO emission was clearly detected, but in contrast to Q0957+561 where we have not yet been able to detect dust emission, HR10 is rich in dust and molecular gas. Although both systems are significantly different, they both independently give crucial insights into an epoch during which the bulk of stars of the present day Universe formed, and thus mark an important phase in galaxy evolution.

Acknowledgements. We are grateful to the referee Jean-Paul Kneib for his valuable comments which have helped to improve the paper. We thank the PdB staff for help with the data reduction. M.K. acknowledges funding support by SFB grant 494. J.M.P. has been partially supported by the Ministerio de Ciencia y Tecnologia under grant numbers ESP2002-01627 and AYA2002-10113-E. P.P. acknowledges partial support by the Spanish Ministerio de Ciencia y Tecnologia under grants ESP2002-01693, ESP2003-04957 and AYA2003-07584.

References

Andreani, P., Cimatti, A., & Loinard, L. 2000, A&A, 354, L1
Angonin-Willaime, M.-C., Soucail, G., & Vanderriest, C. 1994, A&A, 291, 411
Barkana, R., Lehár, J., Falco, E. E., et al. 1999, ApJ, 520, 479
Bernstein, G. M., Fischer, P., Tyson, J. A., & Rhee, G. 1997, AJ, 483, L79
Chae, K.-H. 1999, ApJ, 524, 582
Chartas, G., Chuss, D., Forman, W., Jones, C., & Shapiro, I. 1998, ApJ, 504, 661
Downes, D., & Solomon, P. M. 1998, ApJ, 507, 615
Evans, S. A., Mazzarella, J. M., Surace, J. A., & Sanders, D. B. 2002, ApJ, 580, 749
Falco, E. E., Gorenstein, M. V., & Shapiro, I. I. 1985, ApJ, 289, L1
Grogin, N. A., & Narayan, R. 1996, ApJ, 464, 92
Harvanek, M., Stocke, J. T., Morse, J. A., & Rhee, G. 1997, AJ, 114, 2240
Keeton, C. R., Falco, E. E., Impey, C. D., et al. 2000, ApJ, 542, 74
Kneib, J.-P., Alloin, D., & Pelló, R. 1998, A&A, 339, L65
Kundic, T., Turner, E. L., Colley, E. N., et al. 1997, ApJ, 482, 75
Mediavilla, E., Serra-Ricart, M., Oscoz, A., et al. 2000, ApJ, 531, 635
Papadopoulos, P., Ivison, R., Carilli, C., & Lewis, G. 2001, Nature, 409, 58
Planesas, P., Martín-Pintado, J., Neri, R., & Colina, L. 1999, Science, 286, 2493 (P99)
Sakamoto, K., Okumura, S. K., Ishizuki, S., & Scoville, N. Z. 1999, ApJ, 525, 691
Schneider, P., Ehlers, J., & Falco, E. E. 1992, Gravitational lenses (New York: Springer)
Solomon, P. M., & Barrett, J. W. 1991, IAUS, 146, 235
Solomon, P. M., Downes, D., Radford, S. J. E., & Barrett, J. W. 1997, ApJ, 478, 144
Walsh, D., Carswell, R. F., & Weynman, R. J. 1979, Nature, 279, 381